JOURNAL OF PROPULSION AND POWER
Vol. 19, No. 3, May–June 2003

Characterization of Cryogenic Injection at Supercritical Pressure

Richard Branam[*] and Wolfgang Mayer[†]
German Aerospace Center Lampoldshausen, D-74239 Hardthausen a.K, Germany

This project looks at injection processes of a dense jet simulating oxygen core flow with nitrogen of a coaxial injector used in cryogenic rocket engines. The rocket engine performance is highly dependent on the injection processes such as mixing and jet dissipation of propellants in the supercritical régime. Experimental data at various temperatures and injection velocities taken by Raman imaging and Shadowgraphy were compared to computational models allowing comparisons of density, length scales and jet spreading angles providing insight into mass mixing and jet dissipation. The Raman results are a direct result of the high density gradients and agree well with the expected trend of the computational models but absolute values were 10–25% below expected maximum values in the highest density regions. The jet spreading angle investigation uses several different measuring methods showing agreement with earlier empirical models as well as the computational results. The length scale measurements resulting from the two-point correlation method correspond to calculated Taylor microscales in the developed flowfield. Of the various testing conditions investigated, temperature change proves to affect the jet behavior the most, and in some instances completely changes the character of the jet dissipation and break up.

Nomenclature

C, C_μ = constants
c_p, c_v = coefficient of specific heat constant pressure, constant volume
d = injector diameter (2.2 mm)
$\mathrm{d}\sigma/\mathrm{d}\Omega$ = differential scattering cross section
Fr = Froude number
f = focal length
Gr = Grashof number
g = universal gas constant
I = image intensity, turbulence intensity
I_{Raman} = detected intensity
I_{laser} = laser intensity
K, K_{eff} = thermal conductivity coefficient, effective conductivity coefficient
K_{12} = correlation coefficient for image processing
k, k_T = turbulent kinetic energy, eddy conductivity
L, l = length, length of probe volume
L_{int} = integral length scale
L_{kol} = Kolmogorov length scale
L_{tay} = Taylor microscale
P = pressure
Pr_T = turbulent Prandlt number
q = quantum efficiency of detector (Raman)
Re_d = Reynolds number based on jet diameter and jet density
Re_∞ = Reynolds number based on jet diameter and ambient density
r = radial location
$r_{1/2}$ = radial location of half maximum value of a parameter
T = temperature
u = axial velocity
u', v', w' = turbulence intensity values
$\tilde{u}$ = average turbulence intensity
x = axial location
α = jet divergence angle
γ = ratio of specific heats, c_p/c_v
δ'_{vis} = visible shear layer, rad
δ'_ω = vorticity growth rate, rad
ε = turbulent energy rate of dissipation, optical efficiency
μ = viscosity
ν = kinematic viscosity
ν_T = turbulent eddy viscosity
ρ = density, number density
Ω = solid angle of detection

Subscripts and Superscripts

ax = axial direction
c = centerline value at specified axial location
cr = critical values
d = using the diameter to calculate
rad = radial direction
T = turbulent parameter
0 = centerline value at the injector
∞ = chamber property away from the jet
$*$, $+$ = dimensionless values
$'$ = fluctuation from the mean value
- = average values

Introduction

THERE is much interest in high-pressure combustion for the production of high-power energy conversion and thrust as can be found in diesel engines, gas turbines, and, in particular, rocket engines. These high pressures often exceed the critical pressures of the injected fuel and/or oxidizer. Understanding the complex environment of the rocket chamber to extract the most power requires a good understanding of the mixing and dissipation of the jet. This understanding allows the designer to employ time and cost-saving modeling tools to better design a higher performing engine. Much work has been accomplished in this area as can be seen in Refs. 1–5, but a more complete understanding of the injection process and the development of reliable modeling tools still requires much work.

Presented as Paper 2001-3275 at the AIAA/ASME/ASEE 37th Joint Propulsion Conference and Exhibit, Salt Lake City, UT, 9–11 July 2001; received 2 May 2002; revision received 22 January 2003; accepted for publication 22 January 2003.

[*] Guest Scientist, U.S. Air Force Research Laboratory, Edwards AFB, CA. Member AIAA.

[†] Research Engineer, Head Propulsion Injection Research Group. Member AIAA.

This work takes a step in this direction by looking at cryogenic injection at pressures above the critical pressure and modeling this flow.[6] By the comparison of measured and calculated values, some insight is provided into the behavior of the jet above critical pressures and the modeling effort is validated.

Problem

The experiment injects liquid nitrogen above the critical point (3.39 MPa) through a single, axisymmetric injector into a chamber filled with ambient temperature gaseous nitrogen. The experimental conditions permit examination of the effects of pressure, temperature, and injection speed of the liquid nitrogen into the chamber. Table 1 provides the targeted testing conditions, measured pressures, and temperatures, as well as the average calculated injection velocity for each of the 18 cases investigated. Two-dimensional Raman images were take for the test conditions targeting 120- and 130-K injection temperatures. Because of the high expected density at 100 K, Raman imaging could not produce reliable results for the colder testing conditions.

Shadowgraph images were taken for all conditions and encompassed the area from the injector to 60 mm downstream (approximately 30 injector diameters). The pictures were used to determine density distributions (Raman), jet spreading angles (Raman and shadowgraph), and length scales (shadowgraph). These flow characteristics were compared to computational models for each of the cases. The parameters provide insight into the expected flow dissipation and energy transport of a highly dense oxygen jet in an actual rocket engine.

Cryogenic Jet

A jet flow has three distinct zones, a potential core, a development or transition region, and a self-similar region, as seen in Fig. 1. The potential core contains some portion consisting of only injected fluid and reduces in thickness in the axial direction as the jet mixes with entrained fluid from the surrounding environment. The length of the potential core (x_c/d) is the distance at which the centerline properties remain relatively constant (specifically, density). Schetz[7] suggested there is little or no potential core for fully developed jets. However, he provided an empirical approximation for the length from Harsha[8]:

$$x_c/d = 2.13 Re_d^{0{,}097} \tag{1}$$

These flow conditions are fully developed, turbulent pipe flow ($3.3 \times 10^4 < Re_d < 1.79 \times 10^5$) injected into a pressurized chamber at ambient temperature, but a distinct potential core due to the high densities at the injector is still expected. Chehroudi et al.[9] offered an empirical representation based on the density ratio predicting significantly larger values than the values predicted by Harsha[8] for potential core flow as

$$x_c/d = C(\rho_0/\rho_\infty)^{\frac{1}{2}}, \qquad 3.3 < C < 11 \tag{2}$$

The model offered by Chehroudi et al.[9] is derived from the intact core of liquid sprays but was used for comparison with these supercritical test conditions. After the potential core region, the jet is in a transitional state, which is considered the region of turbulent mixing for a jet. In this region, the energy dissipation and the jet behavior tend to be of the highest interest for mixing purposes. Researchers have indicated the most significant influences on jet development include the velocity ratio between initial jet velocity and the surrounding environment (u_0/u_∞), as well as the density ratio (ρ_0/ρ_∞). These parameters show how the momentum dissipates from the jet into the flowfield. For cryogenic jets, thermal differences also have a significant effect. Looking at temperature and density profiles at various axial locations provides insight into the heat transfer phenomena and its influence on these jets.

At some distance from the injection plane, the jet becomes self-similar. This means a function of only one variable can express the flowfield profiles as no longer varying in the axial direction. Schetz[7] stated that this occurs at approximately $x/d \geq 40$, whereas others have indicated that, for similar jets, velocity profiles exhibit self-similar behavior as close as $x/d \geq 20$ (Ref. 10). Other parameters such as turbulence intensities (u', v', w') may not show this behavior until well after $x/d \geq 200$.

Property Value Comparisons

Nondimensionalizing the flow properties for the radial profiles makes it possible to compare the data for the different testing conditions as follows:

$$\rho^* = (\rho - \rho_\infty)/(\rho_c - \rho_\infty)$$

$$T^* = (T_\infty - T)/(T_\infty - T_c), \qquad u^* = u/u_c \tag{3}$$

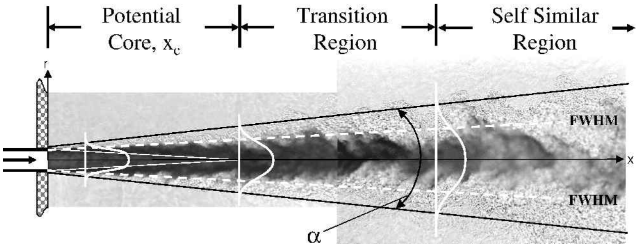

Fig. 1 Jet mixing flowfield.

Table 1 Experimental conditions

Case	Pressure, MPa	Target temperature, K	Target velocity, m/s	Measured pressure, MPa	Injector temperature, K	Average velocity, m/s
1	4	100	2	3.9	104	2.0
2	4	120	2	3.9	122	1.8
3	4	130	2	4.0	132	2.7
4	4	100	5	3.9	103	5.0
5	4	120	5	4.0	123	4.9
6	4	130	5	3.9	133	5.4
7	5	100	2	4.9	104	1.8
8	5	120	2	5.0	123	2.0
9	5	130	2	4.9	132	1.9
10	5	100	5	5.0	102	5.0
11	5	120	5	5.0	123	4.5
12	5	130	5	5.0	132	4.9
13	6	100	2	5.9	105	1.9
14	6	120	2	5.9	123	2.0
15	6	130	2	5.9	132	1.9
16	6	100	5	6.0	104	5.0
17	6	120	5	6.0	123	4.9
18	6	130	5	6.0	132	4.9

The c subscript refers to the centerline or maximum value for the profile and the infinity symbol designates the environmental values. By use of this method, the profiles are 1.0 at the centerline and zero outside the jet itself. Nondimensionalizing length measurements uses the jet diameter d, full width half maximum (FWHM) values $r_{1/2}$, and axial location as indicated.

Comparing the flow properties in the axial direction requires a slightly different nondimensionalizing approach. Density, temperature, and velocity are of particular interest inasmuch as they employ the injection conditions ρ_0, T_0, and u_0 rather than the local centerline values as shown in the following equations:

$$\rho^+ = (\rho - \rho_\infty)/(\rho_0 - \rho_\infty)$$

$$T^+ = (T_\infty - T)/(T_\infty - T_0), \qquad u^+ = u/u_0 \tag{4}$$

Jet Divergence Angle

The jet divergence angle seems to be one of the most highly considered parameters for jet flows. It is easily measured and compared with other results. Chehroudi et al.[11] provided a comparison of many different empirical models with available test data under various conditions. Of particular interest to this experiment were the models put forth by Dimotakis[12] and Papamoschou and Roshko.[13] Dimotakis[12] investigated the entrainment of mass flow into the growing shear layer of a freejet. He proposed a vorticity growth rate equation (to follow), which depends on velocity and density ratio between the fluid flows. For these conditions, the velocity ratio is zero, simplifying the following equation considerably:

$$\delta'_\omega = 0.17\left\{\frac{(1-u_\infty/u_0)}{\left[1+(\rho_\infty/\rho_0)^{\frac{1}{2}}(u_\infty/u_0)\right]}\right\} \times\left(1+\left(\frac{\rho_\infty}{\rho_0}\right)^{\frac{1}{2}}-\frac{\left[1-(\rho_\infty/\rho_0)^{\frac{1}{2}}\right]}{\{1+2.9[(1+u_\infty/u_0)/(1-u_\infty/u_0)]\}}\right) \tag{5}$$

Papamoschou and Roshko[13] proposed a visual thickness equation for incompressible, variable-density mixing layers while studying the turbulence and compressibility effects in plane shear layers. This relationship uses a convective velocity definition to relate the difference in the flows. The experimentally determined constant (0.17) allows results to be compared with axisymmetric jet flows. Again, with velocity ratio zero, the relationship simplifies to

$$\delta'_{\text{vis}} = 0.17\left(1-\frac{u_\infty}{u_0}\right)\frac{\left[1+(\rho_\infty/\rho_0)^{\frac{1}{2}}\right]}{\left[1+(u_\infty/u_0)(\rho_\infty/\rho_0)^{\frac{1}{2}}\right]} \tag{6}$$

Various methods could determine the spreading angle from the computational models. Direct evaluation of the edge of the shear layer using a 0.99 rolloff point for temperature, density, and velocity provides a simple method to accomplish this task. This method can be compared with values determined using an FWHM approach. The edge of the shear layer is difficult to determine from Raman images, and so the procedure is used to determine the location of half of the maximum value and then the value is multiplied by two, as suggested by Chehroudi et al.[11] A similar approach for the computational models also calculate FWHM values to use as a comparison for the Raman results. The shadowgraph images allow direct determination of the angle. These pictures clearly show the edge of the shear layer.

Experimental Setup

Figure 2 shows the pressurized chamber with the injector used in the experiments along with the boundary conditions assumed for the model. The diameter of the injector is 2.2 mm, and the length-to-diameter ratio is greater than 40 which is expected to yield fully developed pipe flow at the injector exit plane. The chamber is equipped with an electronic heater to keep the wall temperature constant. Optical access to the chamber is provided by four windows. The temperature of the injected fluid is targeted at values between 100 and 130 K, the injection velocity can range from 1 to 10 m/s, and the chamber pressure can be as high as 6 MPa. Table 1 shows the data for our test cases.

The temperature of the injected fluid is generally measured at position 1 (T1 in Fig. 3). Because the test setup includes no temperature regulation system, the injection temperature is varied by starting the injection at the ambient temperature of the injector and the piping. During injection, the piping and the injector cool down while the injected fluid heats up. When the temperature of the injected fluid reaches its targeted value at T1, the experiment records the shadowgraph or Raman images. Because the time required to take the images is short compared to the time the injector needs to cool down, the project assumes quasi-steady-state conditions. Nevertheless, there is a certain heat transfer from the injector to the fluid during the measurement resulting in a temperature difference between T1 and T2 (Fig. 3) depending on the injection conditions. To determine the exact injection conditions at T2, calibration measurements at this position were necessary.

A first approach (T2a) used a thermocouple as shown on the left in Fig. 4. The jet is heavily disturbed by the thermocouple, and it is possible the tip of the thermocouple is not completely wetted by the injected nitrogen. Therefore, these measurements were expected to give higher than actual values, providing an upper bound for the expected temperature. A second series of temperature measurements was performed using the setup shown on the right in

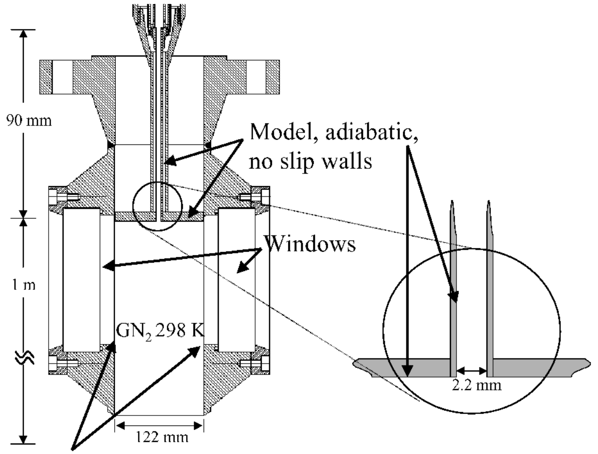

Fig. 2 Test chamber.

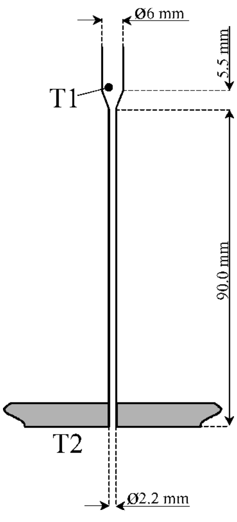

Fig. 3 Injector.

Table 2 Measured temperatures at positions 1 and 2

Case	Pressure, MPa	Target velocity, m/s	Target temperature, K	Measured temperature, T1, K	Temperature T2a, K	Temperature T2b, K
2	4	2	120	120.4	130.0	122.2
3	4	2	130	129.4	140.0	131.9
5	4	5	120	120.9	126.9	122.9
6	4	5	130	130.7	137.0	133.3
8	5	2	120	120.7	131.0	122.6
9	5	2	130	129.8	140.0	131.5
11	5	5	120	120.7	126.2	122.5
12	5	5	130	130.2	135.7	131.7
14	6	2	120	120.7	135.0	122.8
15	6	2	130	129.9	140.5	131.9
17	6	5	120	121.7	128.7	123.3
18	6	5	130	130.8	135.4	132.3

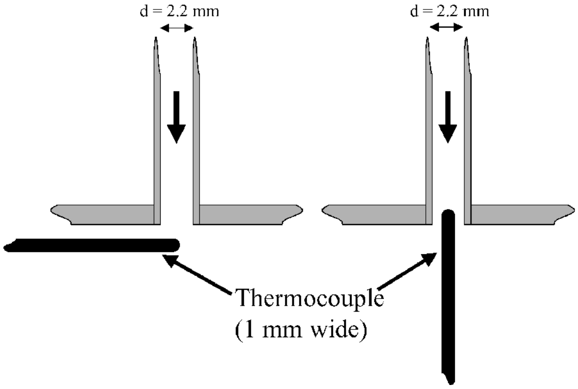

Fig. 4 Temperature measurement at injector exit.

Fig. 4 (T2b), inserting the thermocouple about 1 mm into the injector. These measured temperatures represent the temperature on the jet axis. Because heat transferred from the injector wall to the fluid, a temperature gradient is expected having a maximum temperature at the injector wall and a minimum on the axis. This means the measured temperature is lower than the averaged temperature of the fluid, providing a lower bound. With these measurements made directly in the flow, they are considered more representative. The results of the measurements are shown in Table 2 for several test cases.

Test Data Procedures

Shadowgraphy

The size of the images is approximately 30×20 mm. The procedure digitizes the images with 256 gray levels and a resolution of 2000×1300 pixels corresponding to 15 μm per pixel. Figure 5 shows representative images for two cases. Figure 5a is for case 1, and Fig. 5b is for case 18. Because the test conditions exceed the critical pressure of nitrogen (3.39 MPa), no droplets are seen on any of the images. At low temperatures, the jet is very dense, and not much light can pass through the core of the jet. At raised temperatures, the jet shows a more gaslike behavior. Because the manual evaluation of several hundred images would be very time consuming and exhausting, we developed a computational tool to determine jet spreading angles and visible length scales.

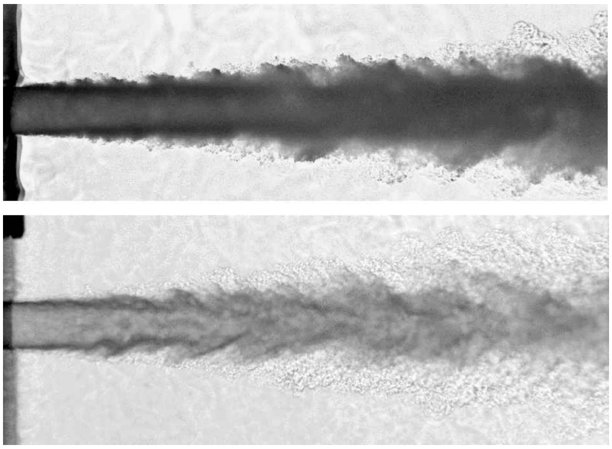

Fig. 5 Shadowgraph images, d = 2.2 mm: a) 3.9 MPa, 104 K, and 2.0 m/s and b) 6.0 MPa, 132 K, and 4.9 m/s.

a) 3.9 MPa, 104 K, and 2.0 m/s

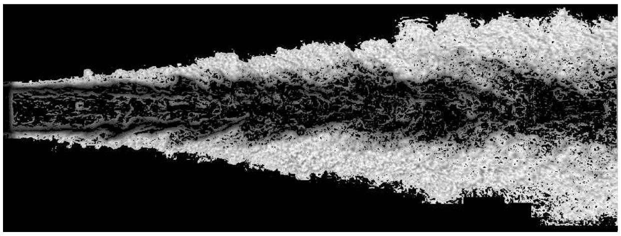

b) 6.0 MPa, 132 K, and 4.9 m/s

Fig. 6 Shadowgraph images after background detection.

Image Processing

The first step was to determine which pixels belong to the jet or the shear layer and which to the background. Therefore, the program divides an image into small squares of 5×5 pixels. The intensity of each pixel within this square consists of a mean value $\bar{I}$ and a fluctuation I' by $I = \bar{I} + I'$. For each square, the program calculates the standard deviation of the intensity. Finally, the process calculates the mean value of the standard deviations of the intensities for each square across all images. For each image, a pixel belongs to the background if the standard deviation of the intensity in the square for that specific pixel is below the mean value of the standard deviation. If so, the intensity is set to zero, which means this pixel is set to black. The frame is set to black as well to avoid the injector being regarded as a part of the jet. The results of this procedure for the images in Fig. 5 are shown in Fig. 6. One can see the program determines regions as background where no jet or spray is visible. Furthermore, parts of the jet where the intensity is almost constant are set as background, isolating only the turbulent shear flow for further analysis. This is a nice feature of the procedure because length scales of the size of the whole image would be calculated in the dark core of the jet otherwise. The spreading angle, then, is fairly easy to determine. With at least 30 shadowgraph images used, the program averages the background images and approximates the upper and lower contours of the jet using the least-squares method. Determining the spreading angle for each image and then averaging the angles was also investigated, but no significant differences were observed.

Evaluation of Visible Length Scales

The two-point correlation method determines the visible length scales for the images. Because the time between taking each image at a given test condition was much larger than the expected timescales for this flowfield, each image is a statistically independent measurement, and each pixel is considered as a single measurement position. All images provide a certain intensity level for each pixel, giving a means to determine length scales using a two-point correlation method. As an example, Fig. 7a, shows a specific pixel location, P1, as well as the intensity for this pixel for each of the images. Figure 7b shows the intensity distribution for pixel P2, which has an axial distance of 5 pixels to P1. The correlation coefficient K_{12} defines the degree of correlation between any two points.

$$K_{12} = \overline{I_1' \cdot I_2'} \Big/ \sqrt{\overline{I_1'^2}} \cdot \sqrt{\overline{I_2'^2}} \tag{7}$$

The result is the correlation factor K_{12} as a function of the distance between two pixels for the entire average image that results from the 30–60 images used for each test case. If the distance between the two pixels is zero, the correlation coefficient is 1. When the distance increases, the correlation coefficient decreases until the signals are not correlated. If pixel P2 belongs to the background, K_{12} is set to zero. Figure 8 shows a plot of K_{12} for pixel P1 (pixel 800) as a function of the pixel number in the x direction. At pixel 800, K_{12} is equal to one and decreases with increasing distance away from this pixel. The average length can be determined by integrating the correlation coefficient as a function of the length over the entire range for these conditions,

$$l = \int_0^\infty K_{12}(l)\,\mathrm{d}l$$

The correlation coefficient as a function of the length results in a somewhat linear relationship for these shadowgraphs. With the K_{12} value having a maximum value of 1.0 and being nearly linear with length, the average length scale then equals the length when $K_{12} = 0.5$. The visible length scales are calculated using $K_{12} = 0.5$ in the axial and radial directions for each pixel instead of integrating for each point, which reduces the amount of computer calculation time required to determine the length considerably. For pixel 800 in Fig. 8, the length scale is being calculated in the axial direction, which results in approximately 20 pixels.

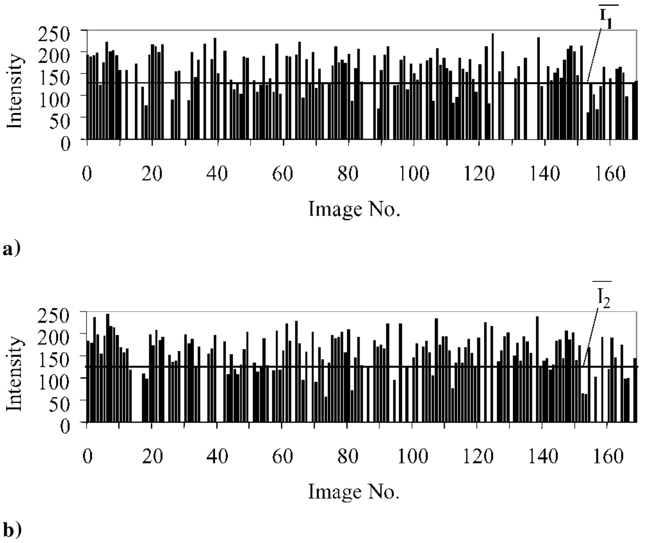

a)

b)

Fig. 7 Intensity profiles, a) P1 and b) P2.

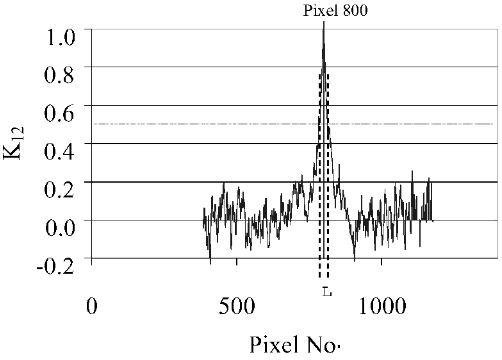

Fig. 8 Correlation coefficient K_{12} for P1.

Furthermore, the program calculates the ratio of the axial to the radial length scales. This gives an indication of whether the visible structures are more circular or elliptical. The numerical calculations use a standard k–ε turbulence model, which assumes isotropic structures. To compare to the model results, a geometric mean value is calculated by $L = \sqrt{[(L_{\mathrm{ax}}^2 + L_{\mathrm{rad}}^2)/2]}$, where L_{ax} and L_{rad} are the length scales in the axial and radial directions, respectively. The numerical models use the k–ε turbulence model parameters to calculated three specific length scales. The Kolmogorov, Taylor, and integral length scales are[14]

$$L_{\mathrm{kol}} = [\nu^3/\varepsilon]^{\frac{1}{4}} \tag{8}$$

$$L_{\mathrm{int}} = k^{\frac{3}{2}} \Big/ \varepsilon \tag{9}$$

$$L_{\mathrm{tay}} = (15\nu\tilde{u}^2/\varepsilon)^{\frac{1}{2}}, \qquad \tilde{u} = [(u'^2 + v'^2 + w'^2/3)]^{\frac{1}{2}} \tag{10}$$

With averaged measured length scales and a dependence on the variations in the intensity levels from the digitized pictures, some uncertainty is expected. The pixel intensity variations from image to image could potentially be a large source of error due to the digital resolution of the length scales. With length scales on the order of 10 pixels, a slight variation in the intensity could cause the length to be miscalculated by one pixel, a 10% error. In actuality, the calculated length scales depend on four different correlation coefficients (two in the axial direction and two in the radial direction). When the actual resolution is calculated taking into account the impact from intensity variations for each of these coefficients, the average length scale deviation ranges only from 2 to 4%.

Another significant source of error is the choice of $K_{12} = 0.5$, assuming the correlation coefficient relationship with length is linear. Variances in the length scale with respect to changes in the correlation coefficient proved to be the major contributor to uncertainty in determining these characteristics. These uncertainty values can be calculated by comparing average length scale values based on $K_{12} = 0.5$ and those calculated by integrating the relationship of K_{12} with respect to the measured length. The contribution to the uncertainty of the average length scales ranges from 3 to 8%. Together with uncertainty from intensity fluctuations, the total expected statistical uncertainty for the length scales falls between 5 and 12%. Figure 9 shows the small differences in the length scales between $K_{12} = 0.5$ (experiment) and integrating (average) for case 5 at $x/d = 20$. The difference is almost indiscernible.

Experimental Approach for Raman Measurements

An abbreviated description of the experimental setup is given here. The setup was described in more detail in the previous campaigns and may be found in Ref. 15. A XeF excimer laser (351 nm) with two independent laser tubes operates in a double oscillator

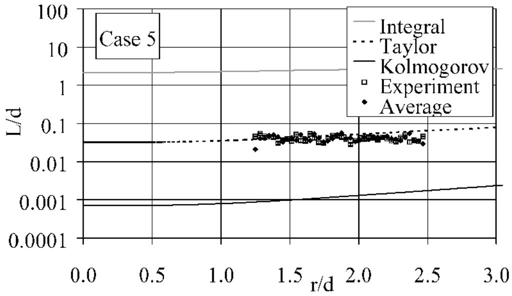

Fig. 9 Comparison between calculated and experimental length scales L_{int}, L_{tay}, and L_{kol} at $x/d = 20$, 4 MPa, 123 K, and 4.9 m/s.

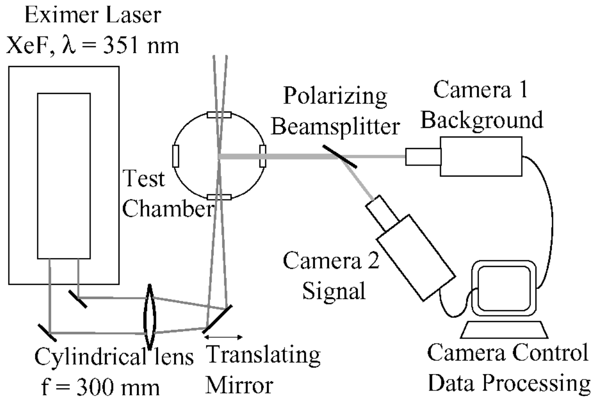

Fig. 10 Raman equipment setup.

configuration. The two laser tubes fire with a short delay to reduce the peak intensity of the laser and to increase the total pulse length to 40 ns. The reduction of the peak power avoids optical damage of the quartz optics and reduces optical breakdown, while the generated Raman signal strength remains constant because the total energy remains unchanged. Both pulses where aligned parallel and focused by a cylindrical quartz lens ($f = 300$ mm) into the chamber (Fig. 10).

To ensure the laser light sheet cuts the cryogenic nitrogen jet directly in the center, it is necessary to precisely align the laser. Therefore, the laser beams are directed by a mirror mounted on a translation stage close to the entrance window. This arrangement allows easy positioning of the light sheet. To form a light sheet with sharp edges, an aperture clips the upper and lower sides of the laser beam. The dimensions of the laser light sheet are 22 mm × 600 μm with total sheet energy of 150 mJ.

Although the upper edge of the sheet is sharply clipped, it is not possible to place the light sheet closer than 2.65 mm to the injector. In spite of the very low diffracted laser power above the sheet, strong scattered light from the metallic injector inhibits a closer positioning of the sheet to the nozzle tip. Two intensified charge-coupled device cameras detect the Raman signal perpendicular to the light sheet. Equipped with identical UV achromatic lenses (Halle, $f = 100$ mm, f/2), the cameras are able to yield a spatial resolution per pixel of approximately 71 μm horizontally × 50 μm vertically. The total image area of the cameras is 37 × 26 mm.

For the correction of the Raman images, it is necessary to separate the Raman signal from any background. Therefore, a polarizing beam splitter separates the detected light into two channels (Fig. 10). The cameras record the reflected beam (polarized perpendicular beam component) and the transmitted beam (parallel polarized light component) separately. The depolarization ratio of nitrogen is only 0.022; therefore, the resonant Raman signal results in a very high polarization. Camera 2 detects this signal. Both cameras 1 and 2 detect the depolarized part of the Raman signal with other nonpolarized background in equal fractions. To obtain the pure resonant Raman signal, the image of camera 1 has to be subtracted pixel by pixel from the image of camera 2 after proper normalization of their respective relative sensitivities.

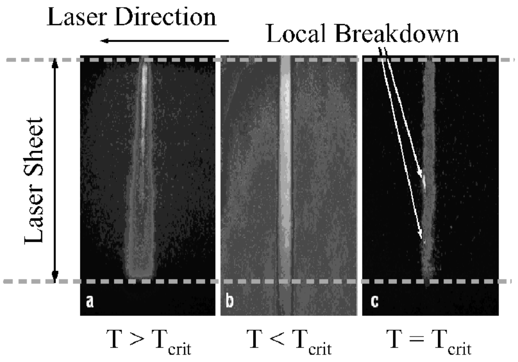

Fig. 11 Laser sheet position in flowfield.

Both cameras are equipped with interference filters with bandwidths (FWHM) of 4 nm. They are only transparent for the resonant wavelength of nitrogen (382 nm) and suppress all other wavelengths by as high as five orders of magnitude reduction. These filters have a peak transmission of only 28%. For this reason, we first tried dielectric filters. They have a peak transmission of more than 70% and a sufficient suppression of the excitation wavelength (transmission $< 5 \times 10^{-4}$). The big disadvantage was they are transparent for wavelengths above approximately 450 nm (visible infrared). There are effects of focusing within the cryogenic jet (like a rod lens) leading to optical breakdown (Fig. 11), as well as reflected and broadband stray light in the chamber exceeding the signal strength of the Raman signal. Even in the part of the image area where no laser sheet is present, we detect signals as high as in the light sheet using dielectric filters (Fig. 11). With combinations of further filters to increase the blocking ratio between 450 and 800 nm, sufficient suppression of the broadband, nonresonant stray light on the camera was still not possible, and therefore, isolation of the Raman signal was not possible with dielectric filters.

The Raman signal is proportional to the number density and to the cross section. When a constant cross section is assumed, the signal intensity is a linear function of the number density. The cameras were easily calibrated when the image areas showed a wide region of bulk gas with temperature and pressure known. Thus, the number density in the jet could easily be extracted from the signal ratio of jet to bulk gas by multiplying by the number density of the surrounding gas.[15] This technique could not be applied on liquid jets for two reasons. First, the Raman cross section of liquid nitrogen is different than gaseous nitrogen.[15,16] Under partially supercritical conditions, there is no reliable way to distinguish in a Raman camera image where the transition lies between liquid and gas and where to apply the cross section of liquid or gaseous nitrogen. Second, the laser power has to be reduced to avoid optical breakdown, and, therefore, the bulk signal is low. For these reasons, we restrict our measurements to supercritical conditions.

In experiments close to critical conditions, it was not possible to avoid optical breakdown completely. In some instances, optical breakdown in small, restricted areas occurs. These small regions, where the light obviously saturates the camera, are taken into account during evaluation by masking these pixels. The number of images recorded for a given experimental condition was small (56 images for each series). Therefore, this procedure is applied only when the number of images discarded due to camera saturation does not exceed 10.

To determine the density from the intensity, a calibration of the images is necessary using the measured temperature and pressure in the ambient gas to determine the ambient gas density. Because the density is a linear function of the intensity (when assuming a constant cross section) the density in the entire image is calculated by $\rho = (I/I_\infty)\rho_\infty$.

Sources of Experimental Error, Raman Images

The Raman signal measuring and data reduction technique are open to significant introduced errors in several ways. One uncertainty is introduced due to optical effects occurring principally in

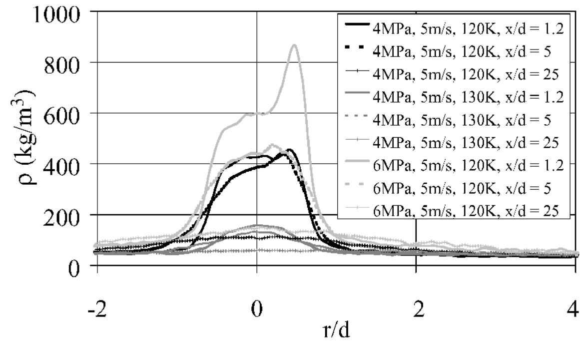

Fig. 12 Measured density, cases 5, 6, and 17.

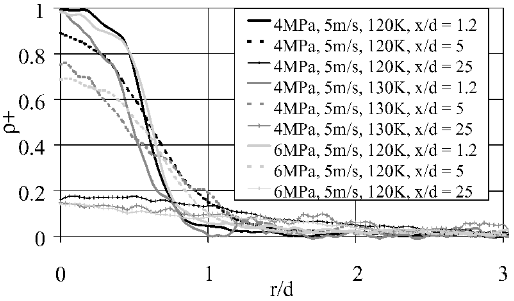

Fig. 13 Measured density, cases 5, 6, and 17.

regions of high refraction index gradients. These refraction index gradients cause disturbances of the light sheet. A round jet focuses the light sheet, causing higher energy intensities in the probe volume, causing plasma formations. The result is the peak seen in the density profiles for 120 K and $x/d = 1.2$ in Fig. 12. Because these peaks are not physically possible, the values past the centerline are considered suspect, and only the entrance side of the light sheet is evaluated.

Another error source from the testing procedure itself, and the ability to determine accurately the injection temperature, can be seen in the maximum density results. Maximum density determined from the Raman images is often lower than the density corresponding to the chamber temperature and pressure. For experimental conditions at 4 MPa, 120 K, and 5 m/s, for example, the maximum measured density is approximately 400 kg/m^3. The expected density is 465 kg/m^3 at 4 MPa and 126.7 K (T2a, Fig. 3). This is an error of 14%. The measured density corresponds to a temperature of 128.5 K at 4 MPa, a difference of only 1.4%, emphasizing the importance of accurately determined temperature values but also suggesting the Raman results are somewhat biased. Farther downstream where the density gradient is not as high, optical effects diminish. The testing procedure also introduces some error due to the quasi-steady-state assumption for the testing. Figure 13 shows a nondimensional plot of the densities from Fig. 12 mirrored at the jet axis. The profiles at $x/d = 1.2$ for the lower temperature are quite similar and show more of a top hat profile as expected, whereas the profile for the higher temperature, case 6, shows a clear density maximum at the jet axis. At the positions farther downstream, $x/d = 5$ and 25, the dimensionless profiles of cases 6 and 17 are quite similar. This indicates an increased heat transfer into the jet at the larger ambient density in case 17. The lack of the top hat profile for case 6 results from the heat transfer from the injector into the injected fluid. The only temperature regulation used here was the heat transfer from the piping and the injector tube into the fluid. The temperature in the liquid nitrogen storage is constant. Therefore, the temperature differences between fluid and injector (heat transfer) are larger at higher injection due to the testing procedure. This causes stronger temperature and density gradients in the injector. The numerical calculations assume a constant temperature of the injected fluid in the injector. Therefore, the influence of the temperature profile in the injector is not considered. This contributes to discrepancies between experimental data and numerical results, but the accuracy of the models proves to be sufficient to compare with the measured values.

The assumption of density as a linear function of the measured intensity introduces some uncertainty in this procedure as well. The image processing takes into account the laser intensity and the efficiency of the detector as seen in the following equation, but adds some variability to our measured density values. A critical point is the scattering cross section. It may change under trans- and supercritical conditions similar to the differences between gases and liquids,

$$I_{\text{Raman}} = I_{\text{laser}}\rho\frac{\mathrm{d}\sigma}{\mathrm{d}\Omega}\Omega\varepsilon q L \tag{11}$$

Furthermore, we found a systematic error at the edges of the images along the axis of the jet. The measured maximum density at both edges exhibits a significant increase. In the streamwise direction, the density cannot physically show an increase for these flow conditions at these locations. This effect is related to the calibration method used to correct the Raman images as well as the optical setup for these tests. As a consequence, the data reduction clipped these values and could only evaluate the center of the images.

Modeling

The modeling for this problem is intended to be used as an engineering tool to compare with experimental results. With use of the CFD-ACE software package, modeling for this multiphysical problem is based on a straightforward computational approach. The flowfield calculations rely on a Favre averaged Navier–Stokes (FANS) flow solver scheme (see Ref. 17). Because the test conditions are in the supercritical regime for nitrogen, real gas nitrogen properties are necessary. The Lee–Kessler,[18] Chung et al.,[19] and modified Benedic–Webb–Rubin model (see Ref. 20) are employed. With the use of real gas properties and low velocity, it is possible to use the incompressible solution scheme and still to take into account the variable density. When a real gas relationship is used for density, coefficient of specific heat at constant pressure, viscosity, and thermal conductivity, the computational model captures the effects of being weakly compressible when the incompressible solution technique, is employed.

The model focuses on a steady-state solution to determine average property distributions for this injection experiment. The orientation of the injector also allows the assumption of negligible body forces. A look at the calculated Grashof, Froude, and Reynolds numbers for this experimental range shows the inertial forces to be the most significant with buoyancy and viscous forces somewhat less critical (see Appendix) reinforcing this assumption.

FANS introduces the Reynolds stresses calculated turbulence using the k–ε model. The model calculations use this high Reynolds approximation in the flow and semi-empirical calculation techniques to determine flow parameters next to the wall where viscous forces are much greater than shear forces.[21] The software package takes into account the contribution of heat transfer from the turbulence by use of a turbulent Prandtl number to determine an effective conductivity coefficient K_{eff}. Mass transfer is handled in the same manner using a turbulent Schmidt number.

$$K_{\text{eff}} = K + (\nu_T \rho c_p / Pr_T) \tag{12}$$

The computational grid used for this problem is a structured, two-dimensional, axisymmetric grid with just over 100,000 cells. The refinement in the injector region is critical. To show grid independence, the same conditions were calculated for one test case using a corser grid and resulted in the same solution. The finer grid was used for all of the test conditions to ensure grid independence at all testing conditions.

The inlet and boundary conditions for this model are very important and extremely sensitive to temperature. Measured mass flow, temperature, and pressure determine the inlet conditions. From the measured values, the initial inlet velocity, turbulent kinetic energy k and rate of dissipation ε are calculated and input to the model.

The outer wall of the chamber is held isothermal by a heater during testing. The injector tube is calculated as an adiabatic wall with the inlet temperature set at expected chamber injection temperatures. To take into account turbulence contributions to heat transfer, the turbulent Prandtl number is set to 1.0 corresponding to Reynolds contention of turbulent-momentum flux and heat flux being of the same order of magnitude (see Ref. 22). The chamber is long enough to consider the outlet to be completely decoupled from the jet flow. Exit velocity is set to agree with total mass inflow of the injector.

Results

Radial Density Profiles

When the progression of the calculated density profiles from $x/d = 1.2$ to 25 are examined, the graphs show the development of the flow as it moves toward a self-similar solution. Figure 14 (case 8) exhibits this trend seen at these testing conditions. The profiles closer to the injector show a flat region ($\rho^* = 1.0$) near the centerline ($r/r_{1/2} = 0$), which eventually no longer exists at $x/d \geq 10$. This corresponds to the potential core. Even though some of the test results show little potential core in the radial profiles, the Raman images do produce measurable core lengths when the axial density profile of the jet is examined. The shadowgraph images show a definite potential core in these regions and provide further validity to the model results, but quantitative results are difficult to obtain.

The transition from a liquidlike jet behavior through the transition region to a fully gaslike jet behavior can be easily seen in the profile after $r/r_{1/2} = 1.0$. When the progression of the jet is followed, using the density profiles from $x/d = 1.2$ to 10, the slope progressively increases. From the profile at $x/d = 10$, the slope then dramatically decreased, and the profiles after this axial location continue to decrease slightly and converge. The profiles for $x/d = 20$ and 25 very nearly share the same line. The experimental data has a considerable amount of variability (no error bars are shown for clarity) but follows the trend of the computational models.

Figure 15 shows another way to see easily the trend for the jet as it moves through the transition region to the self-similar region quickly. Figure 15 shows the density profiles ρ^* as a function of r/x, case 14. The effect of using axial position to normalize the profile radial position shifts the profiles very near the injector to the right and dramatically portrays the expected potential core ($x/d = 1.2$). As the profiles are plotted at intervals away from the injector, the density properties show similar behavior to that shown in Fig. 14. The slope for the entire profile increases until $x/d = 10$ and then begins to decrease again. This is opposite to the behavior in Fig. 14 because of the way the data are presented, but corresponds to the same phenomena. The jet has a high-density core to an axial position near $x/d = 10$, it then goes through a turbulent transition, and then it begins to develop into a self-similar jet flow. The profiles at $x/d = 20$ and 25 do not collapse to the same line; therefore, the relationship suggests the flow has not yet reached self-similarity. The experimental data correspond with this trend again. At $x/d = 1.2$, the very sensitive nature of using axial position to present radial profiles at locations very near the injector causes the difference between the model and experimental data. This representation also suggests the spreading angle of the jet [$\tan(\alpha) = r/x$ at $\rho^* = 0.99$] is initially large and then moves toward a constant value.

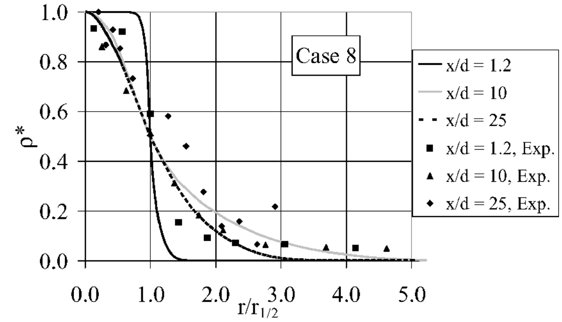

Fig. 14 Density, 5.0 MPa, 123 K, and 2.0 m/s: ——, *x/d* = 1.2; ——, *x/d* = 10; - - -, *x/d* = 25; ■, *x/d* = 1.2, experiment; ▲, *x/d* = 10, experiment; and ◆, *x/d* = 25, experiment.

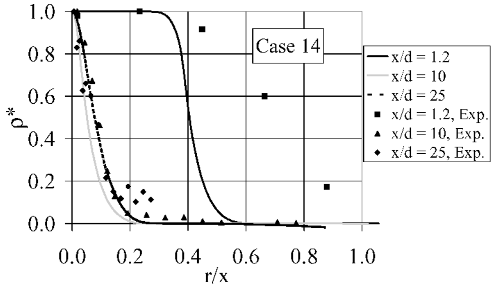

Fig. 15 Density, 5.9 MPa, 123 K, and 2.0 m/s: ——, *x/d* = 1.2; ——, *x/d* = 10; - - -, *x/d* = 25; ■, *x/d* = 1.2, experiment; ▲, *x/d* = 10, experiment; and ◆, *x/d* = 25, experiment.

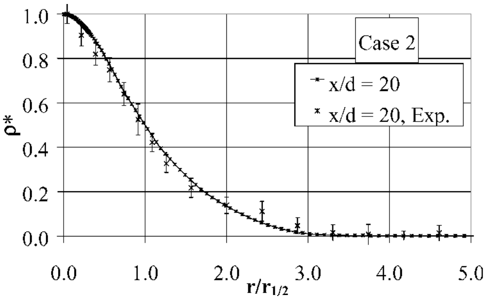

Fig. 16 Density, 3.9 MPa, 122 K, and 1.8 m/s.

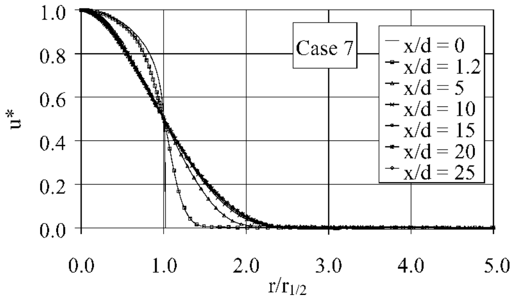

Fig. 17 Velocity, 4.9 MPa, 104 K, and 1.8 m/s.

Figure 16 shows a representative sample of a profile at $x/d = 20$ for case 2 that examines the agreement of the density determined from the Raman images and the calculated model. The experimental deviation was calculated from the values used to get an average density at each location. This difference is a product of the averaging technique and the variability of the data. Figure 16 shows good agreement with the experimental values. For the testing conditions of this paper, the temperature profiles are very similar to the density as mentioned earlier. Because the pressure is nearly constant for each test, density varies only with temperature. Therefore, the temperature shows the same trends seen in the density.

Velocity Profiles

The velocity profiles in the radial direction lend themselves to portraying jet development from the injection point to a fully developed condition better than density or temperature. With inertia dominated (Appendix), the expectation then would be to see these velocity profiles developing rather quickly into self-similar relationships. Figure 17 (case 7) shows the initial velocity to be a fully developed, turbulent pipe flow profile. It develops into a fairly self-similar profile very quickly, and by $x/d = 20$ and 25, the velocity profiles appear to be the same. These later profiles show the edge of the jet to converge to $r/r_{1/2} \approx 2.5$. When all of the profiles in Fig. 16 are considered, the results suggest this value is achieved from an asymptotic relationship from the closer profiles to the more

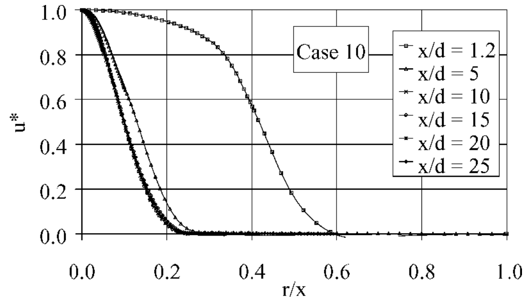

Fig. 18 Velocity, 5.0 MPa, 102 K, and 5.0 m/s.

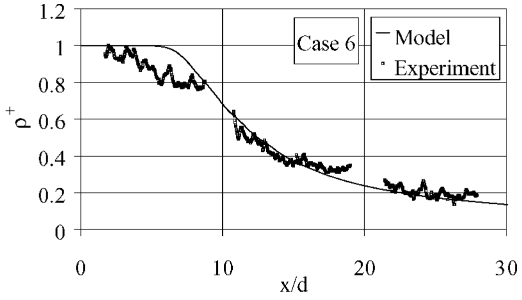

Fig. 19 Centerline density, 3.9 MPa, 133 K, and 5.4 m/s.

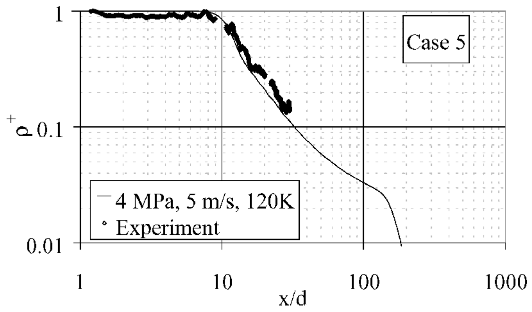

Fig. 20 Centerline density, 4.0 MPa, 123 K, and 4.9 m/s.

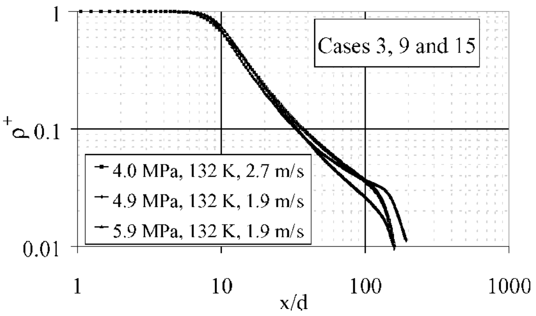

Fig. 21 Centerline density.

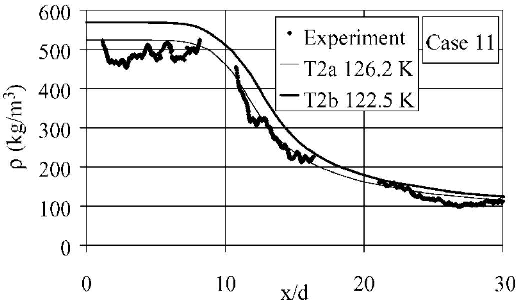

Fig. 22 Centerline density, 5.0 MPa, 123 K, and 4.5 m/s.

distant profiles. In experimental work, this boundary is very difficult to establish.

The velocity profiles of the flow develop much faster than temperature or density distributions for these modeled conditions. Figure 18 (case 10) shows a typical representation of the velocity profiles as well. By $x/d = 10$, the jet appears to be nearly self-similar for velocity, although the jet is not fully developed as seen from the density profiles.

Centerline Density

Primarily, this axial property relationship shows how the jet dissipates with distance from the injector. Observations of the axial density profile provide insight into the behavior of the jet as it moves through the various stages of a jet development. In Fig. 19 (case 6), the computational results present a correlation with the experimental data.

The test results from the Raman images show the centerline density beginning to decrease for test cases at 130 K near the injector, which suggests a very short potential core. An explanation for this phenomenon could be the peak in specific heat. If the temperature is below this peak, the jet is very dense, needing more energy to increase the temperature. Beyond this peak, the density ratio of ambient gas to injected fluid is higher, and the jet dissipates rapidly in the models. For these cases where the temperature is already above the temperature for a maximum specific heat, the density dissipates more smoothly without the flow, needing to absorb a large amount of energy to increase the temperature.

In Fig. 19, the expected characteristics of the potential core are very obvious with the density ratio at approximately one until $x/d = 7.6$ for the model. At this point, the density falls off fairly quickly but does not reach ambient values until much farther downstream ($x/d > 100$). These profiles provide insight into the development of the jet through the various regions when viewed on a logarithmic scale as seen shown in Fig. 20: the potential core, the transition region, and fully developed region.

Figure 20 shows the behavior of a jet (case 5) with a very dense core and the transition to a turbulent mixing zone and then into a fully developed region. The steep slope at $x/d = 10$ to approximately $x/d = 30$ shows the rapid transfer of both momentum and thermal energy. At this point in the jet flow, the density gradient reduces, and the energy dissipation also reduces, which suggests a region of fully developed flow. At a point past $x/d = 150$, the density falls off quickly toward the chamber value, which suggests the jet has almost completely dissipated. The model calculations show this location in the chamber to be the far edge of a recirculation zone established to transfer mass back toward the injector. This mass is the mass entrained in the jet flow from the chamber.

When the computational models are used, the different pressure conditions in the flow (4, 5, and 6 MPa) show little impact on the behavior of the cryogenic jet because these pressure conditions are constant for the chamber and are all above the critical pressure of nitrogen (3.39 MPa). Figure 21 shows the axial density profiles for cases 3, 9, and 15 (target conditions of 130 K and 2 m/s). Even though there is some variation in the Reynolds number, the density profiles follow one another until they are fairly distant from the injector.

One problem in comparing the density measurements from the Raman images with the computational models is to determine accurately the injection temperature, as mentioned earlier but this has proved to be very difficult. This problem is amplified for the test cases near the critical temperature where small changes in the temperature correspond to large changes in the density. The results of the two temperature measuring techniques from Fig. 4 provide a means to bracket the expected Raman results.

Figure 22 shows the difference in the absolute values for density calculated at $T = 122.5$ K and 126.2 K (case 11). When compared to the experimental values, the results of the warmer model calculations show a better agreement. Added to the difficulty of exactly determining the injection temperature, optical effects are suspected of further causing variations in the measured density values. This effect is more pronounced near the injector in the higher density

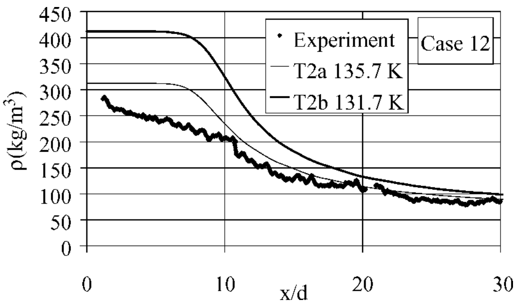

Fig. 23 Centerline density, 5.0 MPa, 132 K, and 4.9 m/s.

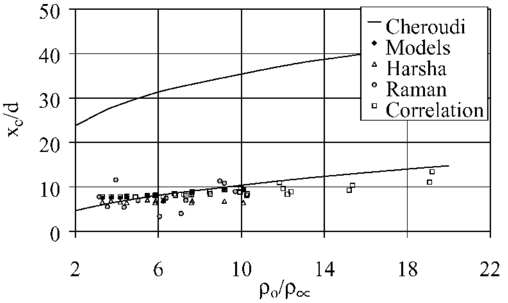

Fig. 24 Core length.

area (x/d from 0 to 10), causing the lower than expected density values from Raman as seen in Fig. 22.

Figure 23 shows warmer injection temperature and a corresponding lower density situation (case 12). Once again, the Raman density values fall below both model results, and the profile has a character similar to that seen in Fig. 19, which suggests little or no potential core for the warmer testing conditions. Farther downstream from the injector, the density values again agree with the model. These results indicate, first, that the heat transfer in the injection tube is significant, particularly in the warmer cases, affecting the length of the potential core and dissipation of the jet. Also, the differences between the Raman density results and the models suggest the Raman images are affected by other optical effects, which results in lower than expected intensity and, therefore, calculated density values. These effects can include signal losses due to absorption and refraction of the Raman signal within the highly dense jet and the assumption of a constant differential scattering cross section of nitrogen for this flow.

Liquid Core Length

The centerline density is a power function of the axial distance from the injector. When plotted on a log–log scale, it is much easier to determine liquid core length and to see the various regions of the jet as in Figs. 20 and 21. The location where the density begins to drop off rapidly determines the liquid core length (x_c/d).

Figure 24 shows the comparison of the values obtained from the calculated models the Reynolds number relationship from Harsha[8] and the relationship offered by Chehroudi et al.,[9] as well as values determined from the two-dimensional Raman images. The two lines identify the range Chehroudi et al. gave for the coefficient in their relationship. The calculated values agree better with the empirical gas relationship suggested by Harsha[8] but tend to fall at or below the lower limit suggested by Chehroudi et al.[9] The core length determined from the Raman images shows a good bit of variability over this density range primarily due to the quality of the two-dimensional Raman images. The experimental values show some deviation from model results but follow the same trend.

The agreement of the core length calculations to a gas jet suggests the cryogenic jet under supercritical pressure behaves very similar to a gas jet, but Harsha's[8] relationship only takes the Reynolds number into account. To consider other factors contributing to these flow conditions, an analytical analysis using the ratio of the specific heats γ, density ratio (ρ_∞/ρ_0), temperature (T_0/T_{cr}), and pressure (P_0/P_{cr}) proves very useful. To separate the interdependence between the Reynolds number and the density ratio, the ambient density is used for the calculation of the Reynolds numbers (Re_∞) in this analysis. The results are exhibited in the following equation as well as in Fig. 24 (correlation). This relationship has a correlation coefficient r of 0.976. The small scaling coefficient (3.344×10^{-5}) suggests the relationship varies very little over these testing conditions. The most significant contributors in this equation are the Reynolds number and density ratio. When the density ratio is very low (very high inlet density), it has a more significant contribution than the Reynolds number, which suggest the temperature ratio would also play a major role. Even though the coefficient for the temperature ratio is large, the range of the temperature ratio (0.8–1.1) limits the influence for these testing conditions. The ratio of specific heats seems to contribute more to the relationship but in an inverse method. At large values for this ratio (near the critical temperature), this relationship reduces the result toward the second constant, 7.363. This relationship can only be considered valid for these testing conditions over the ranges for pressure, temperature, and velocity as defined in Table 1. The equation is

$$x_c/d = 3.344 \times 10^{-5}\, Re_\infty^{0.5597} (\rho_\infty/\rho_0)^{-3.179} \gamma^{-0.9934}$$
$$\times (T_0/T_{\mathrm{cr}})^{5.987} (P_0/P_{\mathrm{cr}})^{-0.5043} + 7.363 \tag{13}$$

Angle of Jet Divergence α

The computational models use two primary methods to determine the angle of jet divergence and apply each to velocity, temperature, and density. The first method uses the FWHM, 50% location values. As suggested by Chehroudi et al,[11] the values are then multiplied by 2 to determine the spreading angle from these radial locations. The second method looks at the 99% rolloff point to determine the jet width. The computational models allow this point to be determined quite easily interpolating the results to achieve precisions smaller than the model grid size when necessary (~0.01 mm). Table 3 shows a comparison of these values along with those determined from the Raman (multiplied by 2) and shadowgraph images. Table 3 and Fig. 25 show a considerable difference between the 50% method and the 99% values. The measuring techniques using the 50% parameter locations result in lower values than those measured by shadowgraph. The results from the 99% parameter locations present fairly consistent results with the shadowgraphs. When considering the possibility the FWHM location does not correspond to half of the jet width, another value for the 2× factor can be calculated. For velocity and temperature, this factor is approximately 2.5, which corresponds nicely with the radial profiles when using $r_{1/2}$ to normalize the radial distance (Fig. 17). The relationship for the density is similar (Fig. 14) but converges to an $r/r_{1/2} \approx 3.0$.

The Raman images lend themselves to determining the FWHM values easier than finding the edge of the jet but unfortunately are not available for the test cases at $T = 100$ K. From the Raman data, the centerline density is quite high, and the jet is quite compact close to the injector exit. Added to this, the temperature difference across the shear layer is small compared with the difference across the

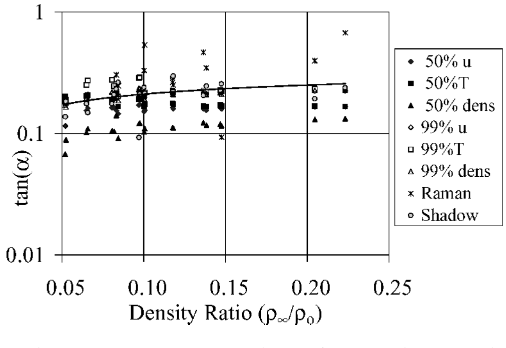

Fig. 25 Divergence angle comparison of measuring techniques: ♦, 50% u; ■, 50% T; ▲, 50% density; ◇, 99% u; □, 99% T; △, 99% density; ⋇, Raman; and ⊙, shadow.

Table 3 Angle of divergence in degrees

Case	ρ_∞/ρ_0	50% u	50% T	50% ρ	99% u	99% T	99% ρ	Raman	Shadow
1	0.0658	9.2	11.6	6.2	11.2	15.3	11.9	——	8.4
2	0.0832	8.8	12.1	8.0	12.0	14.3	13.5	8.4	13.0
3	0.2046	9.4	9.6	7.4	12.6	13.1	12.8	10.8	10.9
4	0.0651	8.8	11.6	5.8	10.3	14.1	11.1	——	10.0
5	0.0845	8.2	9.5	5.2	11.1	11.4	10.6	6.9	14.8
6	0.2233	9.5	9.4	7.5	12.7	13.1	12.9	17.0	13.3
7	0.0818	9.2	10.9	5.9	11.9	13.8	11.7	——	11.8
8	0.1006	8.8	9.9	6.2	11.7	12.3	11.7	14.0	12.0
9	0.1364	9.0	9.6	7.0	12.1	12.7	12.3	12.5	11.6
10	0.0807	9.2	10.7	6.0	12.1	15.4	12.4	——	9.9
11	0.1003	8.6	9.5	5.9	11.3	11.4	10.9	9.1	13.5
12	0.1383	8.8	9.5	6.7	11.9	12.4	11.8	9.6	13.8
13	0.0975	9.8	11.1	6.9	12.5	16.2	13.2	——	11.9
14	0.1177	9.2	10.1	6.4	12.0	12.7	11.9	7.4	16.2
15	0.1467	9.2	9.7	6.8	12.3	12.8	12.2	6.2	12.7
16	0.0971	9.7	10.9	6.9	12.4	16.0	13.3	——	5.3
17	0.1180	9.1	9.9	6.3	12.0	12.4	11.8	7.0	16.5
18	0.1475	9.0	9.6	6.6	12.1	12.5	11.9	2.7	14.3

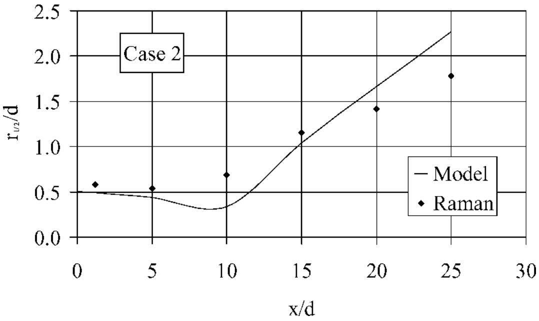

Fig. 26 Density FWHM, 3.9 MPa, 122 K, and 1.8 m/s.

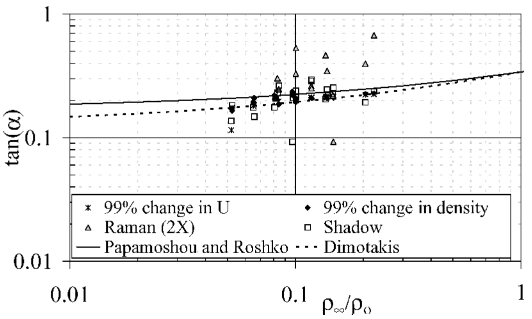

Fig. 27 Jet divergence angle α.

entire jet in this region. Therefore, the dense core of the jet defines the FWHM location instead of the shear layer. The angle is very small close to the injector as determined from $x/d \approx 0\text{–}10$.

In the Raman images for $x/d \approx$ 10–20 and 20–30, the jet warms up and dissipates more. The centerline density in these regions is of the same order of magnitude as the density in the shear layer. Therefore, the FWHM location falls within the shear layer. Comparison with the computational results shows a fairly good agreement Fig. 26. For the colder cases, the angles based on the FWHM are very small or even negative near the injector. For case 2, the minimum value for $r_{1/2}/d$ corresponds with the potential core length ($x_c/d = 8.83$).

The warmer cases do not show this initial decrease in the radial location of the FWHM but similarly have a relatively constant value from the injector until $x/d \approx x_c/d$. When the model results are compared with those from the Raman images, the conclusion then is that the growth rate of the shear layer and the radial distance of the injected fluid moving away from the jet does not correspond to the angle measured from Raman data when the centerline density is significantly higher than the density in the shear layer and ambient gas. Looking at the computational model results and comparing them with the shadowgraph values shows a slightly underpredicted trend, but the 99% rolloff point of the velocity and density shows fairly good agreement. Overall, the values for the warmer cases are significantly better predicted by model calculations than for the colder cases.

Figure 27 shows how the models, Raman images, and shadowgraph images compare with the relationships put forth by Dimotakis[12] and Papamoschou and Roshko.[13] The model calculations and shadowgraph results seem to agree fairly well with the Dimotakis[12] relationship in this density ratio region. The variability of the averaged Raman data is fairly apparent in Fig. 27. Added to Reynolds number, this flow is significantly affected by the ratio of the specific heats γ, density ratio (ρ_∞/ρ_0), temperature (T_0/T_{cr}), and pressure (P_0/P_{cr}) taking into account the heat transfer, supercritical pressure effects, and real gas effects. Performing a dimensionless analysis as similar to the one for core length provides a correlated function for the spread angle using these flow parameters and can only be considered valid for these ranges for pressure, temperature, and velocity as defined in Table 1. The Reynolds number uses the ambient density as before. The following relationship shows the result of this analysis and gives a correlation coefficient r of 0.889:

$$\tan(\alpha) = 0.0498 Re_\infty^{0.0859} (\rho_\infty/\rho_0)^{-0.519} \gamma^{-0.282} (T_0/T_{cr})^{8.05} \times (P_0/P_{cr})^{-1.66} - 0.137 \tag{14}$$

The relative magnitudes for the power coefficients of the different terms suggest the temperature ratio is the significant factor in this relationship. As stated before, the range of testing conditions for this experiment limits the range of the temperature ratio near one, defining a somewhat lesser role in this relationship. This power coefficient (8.05) does show the expected dissipation angle to be less for conditions below the critical temperature. The most significant factor in this relationship is the density ratio. With the power of −0.519, the density ratio is the main contributor in this relationship. Other models have shown the reliance of the angle on the square root of the density ratio but are more often the inverse of the relationship presented here. The power and magnitude make the Reynolds number a very significant part of the relationship, as well reemphasizing a conclusive influence from the inertial forces in divergence angle. When the absolute magnitudes for the pressure ratio and the ratio of specific heat coefficients are considered, the result suggests the contribution from these two parameters is significant but have somewhat less of an impact.

Length Scales

The Taylor microscale (L_{tay}) is considered the dissipation length scale or average length scale where the largest amounts of energy are

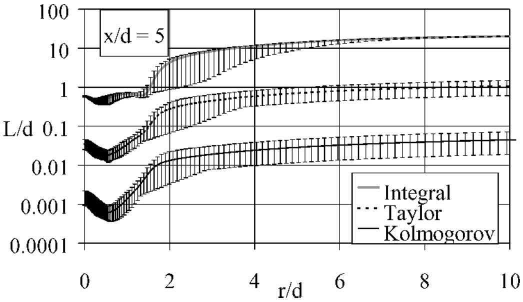

Fig. 28 Calculated length scales L_{int}, L_{tay}, and L_{kol} for all test conditions at $x/d = 5$.

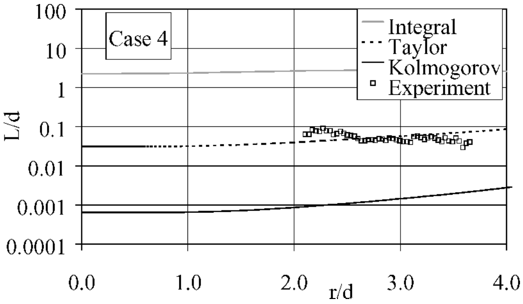

Fig. 29 Comparison between calculated and experimental length scales L_{int}, L_{tay}, and L_{kol} at $x/d = 20$, 3.9 MPa, 103 K, and 5.0 m/s.

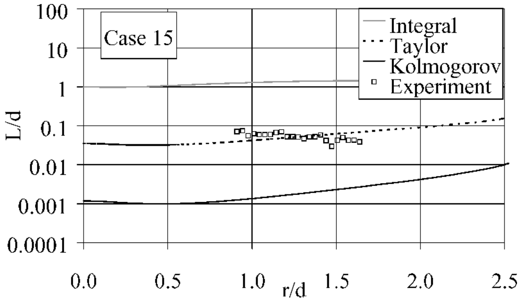

Fig. 30 Comparison between calculated and experimental L_{int}, L_{tay}, and L_{kol} at $x/d = 10$, 5.9 MPa, 132 K, and 1.9 m/s.

being dissipated. The Taylor microscale is bounded by the integral and Kolmogorov length scales and tends to be an order of magnitude greater than the Kolmogorov length scale for these experiments. Although the values vary somewhat, the computational models produce results within a fairly narrow range for each of the length scales. Figure 28 shows average values as well as the maximum and minimum ranges over all test conditions at $x/d = 5$. A local minimum value for the integral length scale (L_{int}) occurs at the edge of the potential core flow and then again at the edge of the shear layer. There are similar characteristics in the other length scales but are not as distinctive as these boundaries. Comparing these results to the geometrically averaged results [$L = \sqrt{(L_{\mathrm{ax}}^2 + L_{\mathrm{rad}}^2)/2}$] from the experimental procedures indicates the visible structures in the flow correspond to the Taylor microscales (Fig. 29, case 4). Near the centerline, the experimental procedure has difficulty providing reliable values for the length scales from the shadowgraphs. This is due to the increased density in this region reducing the light passing through the jet and the optical integration of the jet in the photographs. Figure 30 shows these results for a warmer testing condition (case 15). A quick comparison between Figs. 29 and 30 suggests very little influence on the length scales due to temperature, pressure, or injection velocity under these testing conditions.

With the results of the average values presented in Fig. 28, the conclusion of the measured length scales being relatively constant for these testing conditions is supported and suggests they correspond strongly with the Taylor microscale. The Taylor microscale is an average scale of all of the vorticity lengths expected in the turbulent flowfield. It is defined by average velocity fluctuations and the turbulent energy dissipation. Calculating an average length scale using the two-point correlation method, K_{12}, provides the same representation of the flow using the visible structures in the images for average length scales.

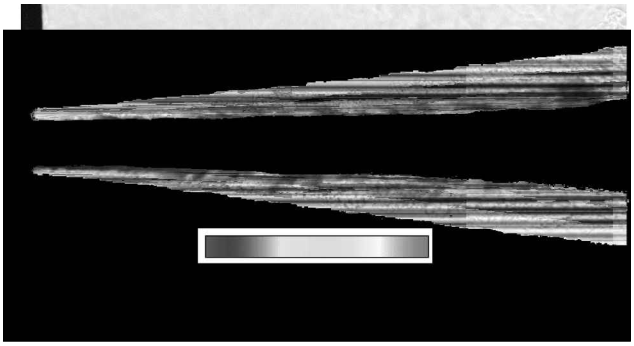

Fig. 31 Axial length scale, case 5, 4 MPa, 123 K, and 4.9 m/s.

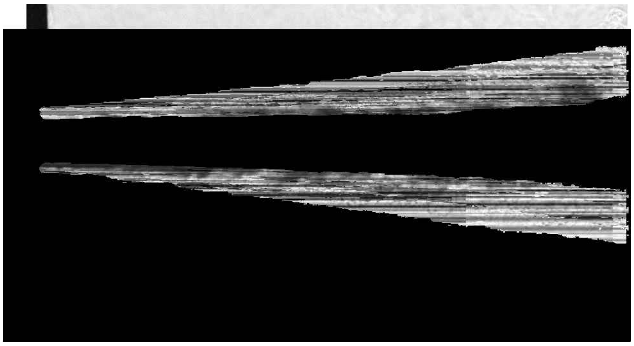

Fig. 32 Radial length scale, case 5, 4 MPa, 123 K, and 4.9 m/s.

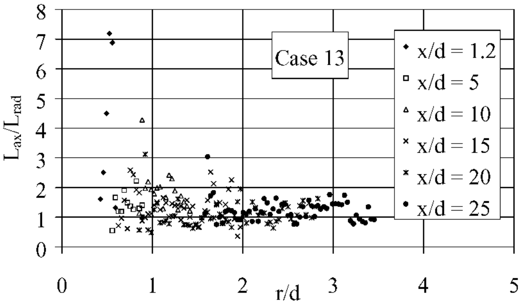

Fig. 33 Mean length scale ratio, 3.9 MPa, 122 K, and 1.8 m/s.

Although the geometrically averaged length determined from the shadowgraphs suggests little influence from temperature, there is actually a distinct influence in the flow near the injector. Figures 31 and 32 show this influence in the axial and radial length scales determined for case 5. The axial length scales closest to the centerline, near the injector, appear much greater than in the higher temperature testing conditions at the same pressure and injection velocity. The radial length scales in Fig. 32 are fairly uniform throughout the flowfield, increasing slightly near the jet centerline. The axial length scales are larger than the radial lengths, which indicates elliptical vortices in the flow. Using the ratio of the axial length to the radial length provides an eccentricity parameter further describing this flow.

Figure 33 shows the profiles for the length scale ratio for case 13 to provide a relative relationship for the measured values. Figure 33 shows for the high-density cases that the visible structures are very elliptical close to the injector ($x/d = 1.2$) and that they approach a more circular form ($L_{\mathrm{ax}}/L_{\mathrm{rad}} \approx 1$) a few jet diameters downstream. For lower density cases (Fig. 34, case 9), the structures close to the

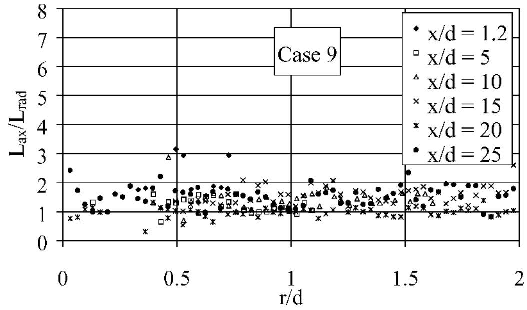

Fig. 34 Mean length scale ratio, 4.9 MPa, 132 K, and 1.9 m/s.

injector are less elliptic than under high-density testing conditions and remain fairly constant downstream. These trends do not seem to be affected by injection velocity or chamber pressure. For these various testing conditions, the only significant influence on the length scales seems to be injection temperature and, therefore, density. At locations near the injector, the turbulent eddies are highly elliptic but become circular motion fairly quickly.

Conclusions

To understand the complex phenomena of a supercritical injection flowfield, a considerable amount of research is still required, but this work provides some insights into several aspects of a rocket injector by examining a single injector using liquid nitrogen above the critical pressure. The various testing conditions considered pressures from 4 to 6 MPa at two target velocities (2 and 5 m/s) and three target injection temperatures (100, 120, and 130 K). Agreement of the numerical results with density, length scales, and jet spreading angles obtained from Raman and shadowgraph images quantitatively validates the computational models.

Under these testing conditions, the velocity, temperature, and density profiles show a distinct trend toward a self-similar jet flow as early as $x/d = 25$. The centerline density profiles in the axial direction provide considerable insight into the jet development from initial core length through to the dissipation of the jet. The core lengths determined from the computational models agree fairly well with the Harsha[8] gas jet empirical approximation and appear to be fairly constant over this density ratio and Reynolds number range. A better empirical model would include other influencing flow parameters, γ, ρ_∞/ρ_0, and T_0/T_{cr} to provide a better correlation with the results.

The flow conditions and specifically density seem to be most affected by temperature variations. The variations in velocity and pressure provide very little if any influence on the flowfield in these operating ranges. The temperature profiles also offer evidence into the expected behavior of the jet spreading angle. These profiles suggest the thermal spreading angle of the jet [$\tan(\alpha) = r/x$] is initially very large near the injection point and then tends toward a constant value.

The various methods for determining the spreading angle prove useful for comparison, but values from the numerical models determined from a 99% rolloff point for velocity agree best with the measured shadowgraph values and the Dimotakis model.[12] From the spreading rate analysis, a further conclusion reached is the growth rate of the shear layer measured from Raman data and the radial distance injected fluid that moves away from the jet are less reliable when the centerline density is significantly higher than the density in the shear layer and the ambient gas. This result is apparent from the FWHM method of determining the spreading angle from the Raman images. The resulting angles from the procedure of multiplying the FWHM values by a factor of two do not correspond with the shadowgraph or the numerical results very well. Length scales measured in the shadowgraphs using a two-point correlation method provide a reasonable method to determine an average length scale for the turbulent structures in the flow. The results of this study show the length scales from the shadowgraphs correspond to the Taylor microscale, an average length scale measure. The shape of the turbulent eddies is also deduced from these calculations and shows them to be more elliptical near the injector, especially for the higher density jets. The turbulence structures, then, become fairly circular a short distance away.

Appendix: Forces Comparison

$$Re_d = \frac{\rho_0 u_0 d}{\mu}, \qquad 33{,}000 < Re_d < 179000$$

$$Fr = \frac{\rho_0 u_0^2}{g(\rho_0 - \rho_\infty)d}, \qquad 2000 < Fr < 18{,}000$$

$$Gr = \frac{g(\rho_0 - \rho_\infty)d^3}{\rho_0 \nu^2} = \frac{Re_d^2}{Fr}, \qquad 400{,}000 < Gr < 2,\ 100{,}000$$

The forces are compared in Table A1.

Table A1 Forces comparison

Pressure, MPa	Target velocity, m/s	Target temperature, K	Re_d	Fr	Gr
4	2	100	3.8×10^4	2,000	800,000
4	2	120	5.9×10^4	2,000	1,700,000
4	2	130	3.4×10^4	3,000	400,000
4	5	100	9.6×10^4	12,000	800,000
4	5	120	1.54×10^5	13,000	1,800,000
4	5	130	1.79×10^5	18,000	1,800,000
5	2	100	3.3×10^4	2,000	700,000
5	2	120	5.9×10^4	2,000	1,700,000
5	2	130	6.7×10^4	2,000	2,000,000
5	5	100	9.5×10^4	12,000	700,000
5	5	120	1.42×10^5	13,000	1,600,000
5	5	130	1.7×10^5	14,000	2,100,000
6	2	100	3.6×10^4	2,000	700,000
6	2	120	5.6×10^4	2,000	1,500,000
6	2	130	6.3×10^4	2,000	1,800,000
6	5	100	9.3×10^4	13,000	700,000
6	5	120	1.35×10^5	13,000	1,400,000
6	5	130	1.61×10^5	13,000	2,000,000

Acknowledgments

This work is supported by the Federal Ministry of Education and Research under Contract 50TT9627 (Project TEKAN). The project was accomplished in the framework of the Atomization and Spray Processes Project under the guidance of Deutsche Forschungsgemeinschaft.

References

[1] Mayer, W., and Tamura, H., “Propellant Injection in a Liquid Oxygen/Gaseous Hydrogen Rocket Engine,” *Journal of Propulsion and Power*, Vol. 12, No. 6, 1996, pp. 1137–1147.

[2] Ivancic, B., Mayer, W., Krülle, G., and Brüggemann, D., “Experimental and Numerical Investigation of Time and Length Scales in LOX/GH2-Rocket Combustors,” AIAA Paper 99-2211, June 1999.

[3] Candel, S., Herding, G., Snyder, Scouflaire, P., Rolon, C., Vingert, L., Habiballah, M., Grisch, F., Péalat, M., Bouchardy, P., Stepowski, D., Cessou, A., and Colin, P., “Experimental Investigation of Shear Coaxial Cryogenic Jet Flames,” *Journal of Propulsion and Power*, Vol. 14, No. 5, 1998, pp. 826–834.

[4] Mayer, W., Schik, A., Schäffler, M., and Tamura, H., “Injection and Mixing Processes in High-Pressure Liquid Oxygen/Gaseous Hydrogen Rocket Combustors,” *Journal of Propulsion and Power*, Vol. 16, No. 5, 2000, pp. 823–828.

[5] Mayer, W., “TEKAN-Research on Cryogenic Rocket Engines at DLR Lampoldshausen,” AIAA Paper 2000-3219, July 2000.

[6] Mayer, W., Schik, A., Vieille, B., Chaveau, C., Goekalp, I., Talley, D., and Woodward, R., “Atomization and Breakup of Cryogenic Propellants Under High-Pressure Subcritical and Supercritical Conditions,” *Journal of Propulsion and Power*, Vol. 14, No. 5, 1998, pp. 835–842.

[7] Schetz, J. A., *Injection and Mixing in Turbulent Flow*, Progress in Aeronautics and Astronautics, Vol. 68, AIAA, New York, 1980, pp. 19–84.

[8] Harsha, P. T., "Free Turbulent Mixing: A Critical Evaluation of Theory and Experiment," *Turbulent Shear Flows*, CP-93, AGARD, 1971.

[9] Chehroudi, B., Talley, D., and Coy, E., "Initial Growth Rate and Visual Characteristics of a Round Jet into a Sub- to Supercritical Environment of Relevance to Rocket, Gas Turbine, and Diesel Engines," *37th AIAA Aerospace Sciences Meeting and Exhibit*, AIAA, Reston, VA, 1999, pp. 6, 7.

[10] Schlichting, H., *Boundary-Layer Theory*, McGraw–Hill, New York, 1979, pp. 729–755.

[11] Chehroudi, B., Cohn, R., Talley, D., and Badakhshan, A., "Raman Scattering Measurements in the Initial Region of Sub- and Supercritical Jets," *36th AIAA/ASME/SAE/ASEE Joint Propulsion Conference and Exhibit*, AIAA, Reston, VA, 2000, pp. 3–10.

[12] Dimotakis, P. E., "Two-Dimensional Shear-Layer Entrainment," *AIAA Journal*, Vol. 24, No. 11, 1986, pp. 1791–1796.

[13] Papamoschou, D., and Roshko, A., "The Compressible Turbulent Shear Layer: An Experimental Study," *Journal of Fluid Mechanics*, Vol. 197, 1988, pp. 453–477.

[14] Finzenhagen, F., O'Doherty, T., Bates, C., Kremer, H., and Wirtz, S., "Statistical Analysis of PIV Data and Determination of Small Turbulent Scales in Highly Turbulent Flows," *3rd International Workshop on Particle Image Velocimetry*, Univ. of California, Santa Barbara, 1999, pp. 519–525.

[15] Decker, M., Schik, A., Meier, U. E., and Stricker, W., "Quantitative Raman Imaging Investigations of Mixing Phenomena in High-Pressure Cryogenic Jets," *Applied Optics*, Vol. 37, No. 24, 1998, pp. 5620–5627.

[16] Eckhardt, G., and Wagner, W. G., "On the Calculation of Absolute Raman Scattering Cross Sections from Raman Scattering Coefficients," *Journal of Molecular Spectroscopy*, Vol. 19, 1966, pp. 407–411.

[17] Cebeci, T., and Smith, A. M. O., *Analysis of Turbulent Boundary Layers*, Academic Press, New York, 1974.

[18] Lee, B. I., and Kesler, M. G., "A Generalized Thermodynamic Correlation Based on Three-Parameter Corresponding States," *AIChE Journal*, Vol. 21, May 1975, p. 510.

[19] Chung, T. H., Ajlan, M., Lee, L. L., and Starling, K. E., "Generalized Multiparameter Correlation for Nonpolar and Polar Fluid Transport Properties," *Industrial and Engineering Chemistry Research*, Vol. 27, No. 4, 1988, pp. 671–679.

[20] Younglove, B. A., "Thermophysical Properties of Fluids," *Journal of Physical Chemistry*, Reference Data 11: Supplement 1, 1982.

[21] Launder, B. E., and Spalding, D. B., "The Numerical Computation of Turbulent Flows," *Computational Methods Applied Mechanical Engineering*, Vol. 3, 1974, pp. 269–289.

[22] White, F. M., *Viscous Fluid Flow*, 2nd Ed., McGraw–Hill, New York, 1991, Chap. 6, p. 482.